Redundant and specific roles of cohesin STAG subunits in chromatin looping and transcriptional control

Valentina Casa,[1,6] Macarena Moronta Gines,[1,6] Eduardo Gade Gusmao,[2,3,6] Johan A. Slotman,[4] Anne Zirkel,[2] Natasa Josipovic,[2,3] Edwin Oole,[5] Wilfred F.J. van IJcken,[1,5] Adriaan B. Houtsmuller,[4] Argyris Papantonis,[2,3] and Kerstin S. Wendt[1]

[1]Department of Cell Biology, Erasmus MC, 3015 GD Rotterdam, The Netherlands; [2]Center for Molecular Medicine Cologne, University of Cologne, 50931 Cologne, Germany; [3]Institute of Pathology, University Medical Center, Georg-August University of Göttingen, 37075 Göttingen, Germany; [4]Optical Imaging Centre, Erasmus MC, 3015 GD Rotterdam, The Netherlands; [5]Center for Biomics, Erasmus MC, 3015 GD Rotterdam, The Netherlands

Cohesin is a ring-shaped multiprotein complex that is crucial for 3D genome organization and transcriptional regulation during differentiation and development. It also confers sister chromatid cohesion and facilitates DNA damage repair. Besides its core subunits SMC3, SMC1A, and RAD21, cohesin in somatic cells contains one of two orthologous STAG subunits, STAG1 or STAG2. How these variable subunits affect the function of the cohesin complex is still unclear. STAG1- and STAG2-cohesin were initially proposed to organize cohesion at telomeres and centromeres, respectively. Here, we uncover redundant and specific roles of STAG1 and STAG2 in gene regulation and chromatin looping using HCT116 cells with an auxin-inducible degron (AID) tag fused to either STAG1 or STAG2. Following rapid depletion of either subunit, we perform high-resolution Hi-C, gene expression, and sequential ChIP studies to show that STAG1 and STAG2 do not co-occupy individual binding sites and have distinct ways by which they affect looping and gene expression. These findings are further supported by single-molecule localizations via *direct* stochastic optical reconstruction microscopy (*d*STORM) super-resolution imaging. Since somatic and congenital mutations of the STAG subunits are associated with cancer (STAG2) and intellectual disability syndromes with congenital abnormalities (STAG1 and STAG2), we verified STAG1-/STAG2-dependencies using human neural stem cells, hence highlighting their importance in particular disease contexts.

[Supplemental material is available for this article.]

Cohesin is a multiprotein complex with fundamental roles in genome stability and spatial chromatin organization within the cell nucleus. The ring-shaped complex consists of the core subunits SMC3, SMC1A, RAD21 (Smc3, Smc1 and Scc1 in *Saccharomyces cerevisiae*) and one SA/STAG (Stromal Antigen) subunit (Scc3 in *S. cerevisiae*). Transiently interacting subunits and regulators are PDS5A/PDS5B (Pds5 in *S. cerevisiae*), CDCA5 (also known as sororin), WAPL, NIPBL, and MAU2 (Nishiyama 2019).

Vertebrates have three STAG orthologs—STAG1 (also known as SA1), STAG2 (also known as SA2), and STAG3, with STAG3 only expressed in germ cells and certain cancers (Prieto et al. 2001; Winters et al. 2014). STAG1 and STAG2 are ubiquitously expressed in somatic cells at varying ratios between cell types and are mutually exclusive (Losada et al. 2000). STAG1 and STAG2 display high protein similarity (~75% conserved) with only their N and C termini diverging (30%–50% homology) (Losada et al. 2000; Kong et al. 2014).

Previously, STAG1 and STAG2 were reported to be differentially required for sister chromatid cohesion at telomeres and centromeres, respectively (Canudas and Smith 2009), while both contribute to chromosome arm cohesion (Remeseiro et al. 2012). STAG1-null mouse embryonic fibroblasts show increased aneuploidy resulting from telomeric cohesion defects (Remeseiro et al. 2012). STAG1 also protects chromosome ends and promotes replication by facilitating restart of stalled replication forks (Canudas and Smith 2009; Deng et al. 2012; Remeseiro et al. 2012). Acute STAG2 depletion results in partial loss of centromeric cohesion (Canudas and Smith 2009; Remeseiro et al. 2012; Lennox and Behlke 2016; Busslinger et al. 2017). STAG2 is also required for DNA damage repair via homologous recombination in the S/G2 phases (Kong et al. 2014), while both STAG1 and STAG2 are necessary for the S-phase DNA damage checkpoint (Kong et al. 2014). Cells can tolerate the absence of STAG1 or STAG2 but not of both, suggesting partial redundancy in their roles (Hill et al. 2016; Benedetti et al. 2017; van der Lelij et al. 2017).

Besides their apparent functional differences, cohesin complexes containing STAG1 or STAG2 colocalize with the CTCF chromatin insulator along mouse and human chromosomes (Rubio

et al. 2008; Wendt et al. 2008; Remeseiro et al. 2012). Cohesin and CTCF form chromatin loops by tethering distant genomic regions (Hadjur et al. 2009; Nativio et al. 2009; Zuin et al. 2014a; Nora et al. 2017; Rao et al. 2017), preferentially sites with convergently oriented CTCF motifs (Rao et al. 2014). Partitioning of the genome into loop clusters, known as topologically associating domains (TADs) (Dixon et al. 2012; Nora et al. 2012), impacts gene regulation by facilitating/abrogating promoter-enhancer contacts. How STAG1- and STAG2-cohesin are each involved in shaping these loops remains unclear. Decoding this will not only complete our understanding of cohesin molecular functions but also allow us to better understand pathologies linked to these orthologs. STAG2 is frequently mutated in different cancer types, such as urothelial bladder carcinoma (Balbás-Martínez et al. 2013; Solomon et al. 2013), Ewing sarcoma (Brohl et al. 2014; Tirode et al. 2014), and acute myeloid leukemia (Rocquain et al. 2010). Congenital loss-of-function mutations in STAG1 or STAG2 cause intellectual disability disorders which do not recapitulate the full spectrum of Cornelia de Lange syndrome (CdLS), the major cohesin-related disorder (Lehalle et al. 2017; Mullegama et al. 2017; Soardi et al. 2017).

Here, we combine chromatin genomics, in Hi-C and ChIP-seq, with single-molecule approaches, in *direct* stochastic optical reconstruction microscopy (*d*STORM) imaging, to decipher the individual contributions of STAG1 and STAG2 in the 3D genome organization at different scales.

Results

Acute auxin-inducible degradation of STAG1 and STAG2 in human diploid cells

To obtain cells allowing for rapid depletion of either STAG1 or STAG2 and their visualization and immunopurification, we inserted the mini auxin-inducible degron (AID) tag in frame with mClover at the 3′ ends of the *STAG1* and *STAG2* open reading frames in HCT116-CMV-OsTIR1 cells (hereafter STAG1-AID and STAG2-AID) (Fig. 1A,B; Natsume et al. 2016). Earlier reports in RAD21-AID cells show that leakiness of the system yields lower levels of AID-tagged proteins compared to wild type (Natsume et al. 2016; Yesbolatova et al. 2019). To minimize this, we optimized our culturing conditions by using charcoal/dextran (C/D)-treated serum (Supplemental Fig. S1A–D). Nonetheless,
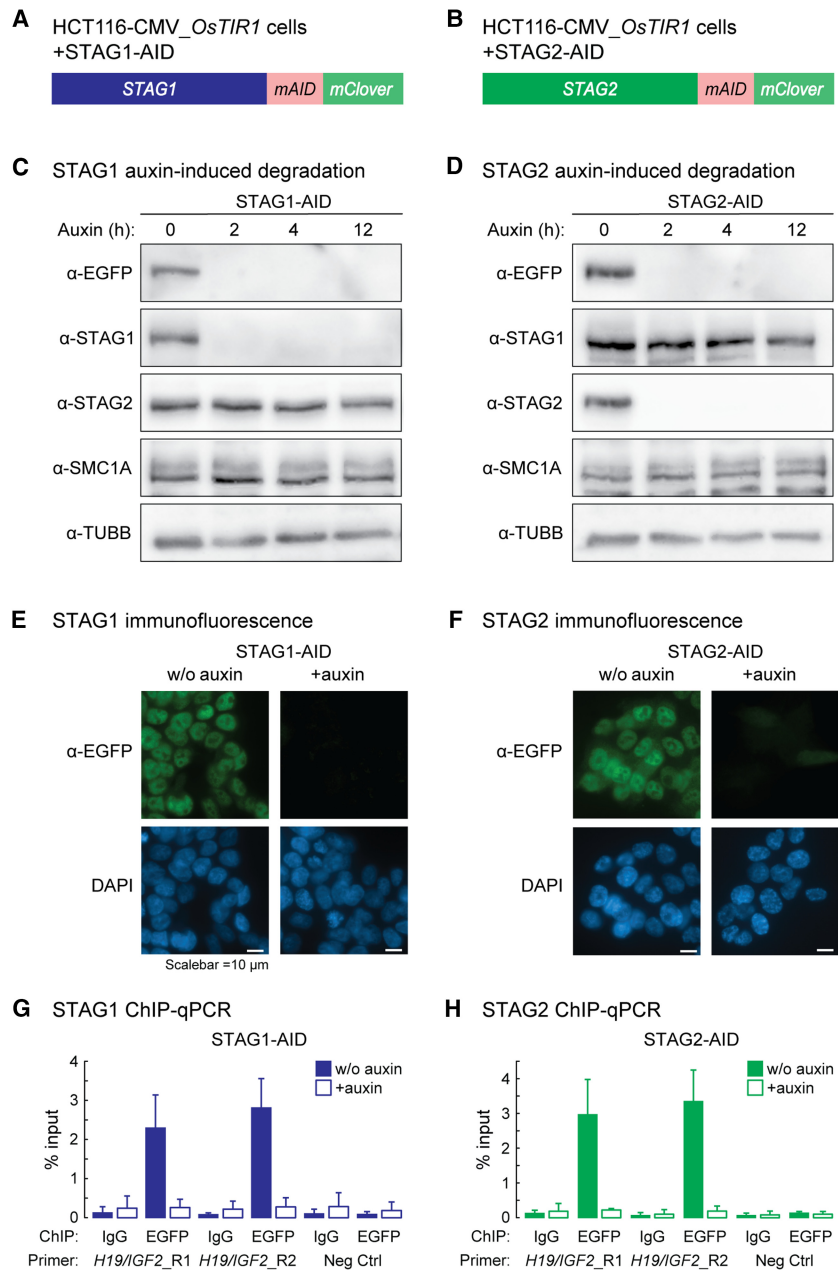
and just like in the case of RAD21-AID cells (Rao et al. 2017), reduced STAG1/2 titers would not affect the outcome of experimental comparisons performed in these lines in the presence/absence of degradation stimuli via auxin.

Cohesin immunoprecipitation confirmed that STAG1- and STAG2-AID incorporate into the complex (Supplemental Fig. S1E,F). Both are quantitatively degraded upon auxin treatment

Figure 1. Acute auxin-inducible degradation of STAG1 and STAG2. (*A,B*) Schematic of the CRISPR-mediated modification of STAG1 (*A*) and STAG2 (*B*) to add a mini auxin-inducible degron tag (mAID) and a mClover tag to the C termini of STAG1 and STAG2 in HCT116-CMV-OsTIR1 cells. (*C,D*) Addition of auxin leads to a degradation of STAG1-AID (*C*) and STAG2-AID (*D*) within 2 h without affecting the protein level of the respective other ortholog. (*E,F*) Visualization of the STAG1-AID (*E*) and STAG2-AID (*F*) degradation 12 h after auxin addition by immunostaining. (*G,H*) ChIP-qPCR with anti-EGFP antibodies (detects mClover) shows efficient depletion of STAG1-AID (*G*) and STAG2-AID (*H*) from cohesin sites in the H19/IGF2 locus.

for 12 h (Fig. 1C–F), without reciprocally affecting the levels of the nontargeted STAG subunit or of SMC1A (Fig. 1C,D; Supplemental Fig. S1G), and ChIP-qPCR confirmed that STAG1- or STAG2-AID were fully removed from chromatin (Fig. 1G,H).

STAG1 and STAG2 have overlapping and discrete binding positions on chromatin

To obtain a comprehensive repertoire of STAG1 and STAG2 binding on chromatin, we performed ChIP-seq using antibodies

against EGFP, detecting the mClover-tag (Natsume et al. 2016). We identified 17,615 and 13,524 robust binding sites for STAG1 and STAG2, respectively (q-value < 0.005) (Fig. 2A). More than 60% of these binding sites are shared STAG1 and STAG2 sites (STAG1/2), whereas 4650 sites were exclusively called for STAG1 (STAG1-only) and 568 sites for STAG2 (STAG2-only), respectively (Fig. 2B). A comparison with published ChIP-seq data from a different human cell type (MCF10A) obtained with custom-made anti-STAG1 and -STAG2 antibodies (Kojic et al. 2018) showed that STAG1- and STAG2-peaks are partially conserved between the
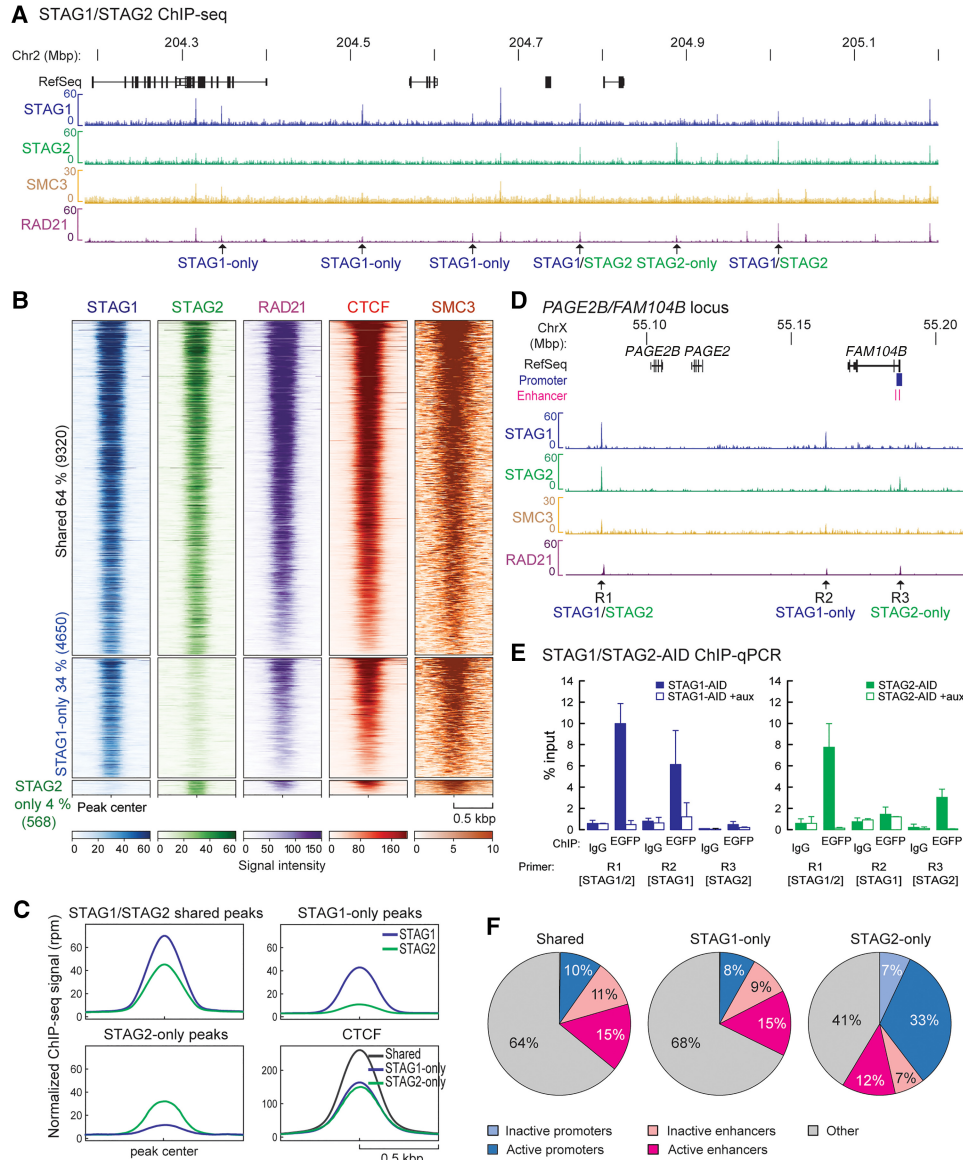

Figure 2. STAG1 and STAG2 have overlapping as well as discrete binding positions on chromatin. (A) ChIP-sequencing profiles of STAG1 and STAG2 from STAG1-AID and STAG2-AID cells using anti-EGFP antibodies (merge of two replicates), SMC3 ChIP-sequencing for STAG1-AID cells and published RAD21 ChIP-seq data from RAD21-AID cells (Rao et al. 2017) are displayed. Examples of STAG1-only, STAG2-only, and STAG1/2 shared sites are indicated. (B) Heat maps showing the ChIP-seq signals for STAG1, STAG2, RAD21, CTCF, and SMC3 in common and -only sites. RAD21 and CTCF ChIP-seq data are from Rao et al. (2017). (C) Averaged signal intensity of STAG1, STAG2 and CTCF (Rao et al. 2017) on STAG1/2 common sites and STAG1-/STAG2-only sites. (D) Examples of STAG1 and STAG2 binding sites in the PAGE2B/FAM104B locus that were tested in (E) by ChIP-qPCR. (E) Efficiency of auxin-mediated degradation was tested by ChIP-qPCR for different STAG1/STAG2 sites. (F) Localization of STAG1/STAG2 common sites or STAG1- or STAG2-only sites to inactive/active promoters or active/inactive enhancers based on the presence of characteristic histone modifications (Supplemental Table S7). The percentage of the sites in the different regions is indicated.

two cell types but display also cell type–specific peaks (Supplemental Fig. S2A–C). Nonetheless, all our STAG1- and STAG2-sites expectedly aligned to cohesin (SMC3 and RAD21), as well as to CTCF sites (RAD21 and CTCF from RAD21-AID cells) (Fig. 2B; Supplemental Fig. S3A,B; Natsume et al. 2016; Rao et al. 2017). The overall signal intensity of CTCF, but also STAG1 and STAG2, at STAG1/STAG2 common peaks was higher than in STAG1-only and STAG2-only peaks, possibly indicating lower occupancy at this subset of sites (Fig. 2C). We confirmed subunit-specific binding of STAG1 and STAG2 at STAG1-/STAG2-only sites using ChIP-qPCR, which was abolished upon auxin treatment only for the relevant subunit (Fig. 2D,E; Supplemental Fig. S3D–G), with SMC3 (cohesin core subunit) recruitment decreasing accordingly (Supplemental Fig. S3C,E,G).

We next asked whether one STAG subunit replaced the other following degradation. STAG1 ChIP-qPCR in STAG2-AID cells showed such reciprocal replacement at every STAG1/2 site, with an average 1.5-fold increase after STAG2 degradation. Conversely, STAG2-only sites showed less, if any, enrichment for STAG1 (Supplemental Fig. S3H,I). When STAG2 ChIP-qPCR was performed after STAG1 degradation, STAG2 could only minimally, if at all, substitute STAG1 (Supplemental Fig. S3J,K). To address this discrepancy between STAG1- and STAG2-only sites, we looked into their distributions across the genome, focusing on regulatory regions. Almost 10% of the STAG1/2 common sites are found at active gene promoters and 15% at active enhancers. STAG1-only sites show a similar distribution—8% at active promoters and 15% at active enhancers—while significantly larger fractions of STAG2-only sites were at active promoters (33%) and enhancers (12%) ($p < 0.001$, Fisher's exact test) (Fig. 2F; Supplemental Table S7). Analysis of transcription factor (TF) motifs contained in DNase I-hypersensitive footprints under all STAG1/STAG2 and STAG1-/STAG2-only peaks showed that they potentially cobind with diverse and nonoverlapping repertoires of TFs (Supplemental Fig. S4A,D). GO-term analysis using Metascape (Zhou et al. 2019) revealed that these TFs are implicated in development and differentiation processes (Supplemental Fig. S4B). Using published ChIP-seq data from HCT116 cells (Supplemental Table S8), we showed that STAG2 peaks associate more with H3K4me3, indicative of active promoters, and less with H3K4me1 signal, indicative of enhancers (Supplemental Fig. S4C; in line with Fig. 2F). We could also confirm the prediction of different cobound TFs at STAG1- and STAG2-only sites, like FOSL1 of the FOS/JUN family at STAG1-only peaks (Supplemental Fig. S4C,D).

STAG1 and STAG2 do not cobind at individual binding sites

STAG1 and STAG2 ChIP-seq peaks overlap at >60% of sites, but it is unclear whether STAG1- and STAG2-containing complexes indeed localize together or whether this reflects the average of nonoverlapping binding in the cell population. To address this, we performed sequential ChIP ("Re-ChIP") (Fig. 3A), first using antibodies against STAG2, EGFP (mClover), or SMC3 to ChIP from HCT116-STAG1-AID cells. The antibodies were crosslinked to beads to avoid carry-over into the second ChIP. From these ChIP eluates, a second ChIP with antibodies against STAG1 or STAG2 was performed. We could not ChIP STAG1 from the eluate of the STAG2-ChIP and, vice versa, STAG2 from the STAG1 ChIP eluate (Fig. 3B,C; Supplemental Fig. S5). However, using a SMC3 ChIP eluate, both STAG1- and STAG2-antibodies yielded strong ChIP-qPCR enrichments (Fig. 3B,C). Thus, STAG1-cohesin and

STAG2-cohesin seem to not co-occupy the same site on the individual DNA strands.

We followed this up by single-molecule localization studies using triple-color dSTORM (van de Linde et al. 2011), allowing for the localization of single molecules with ~25-nm precision. We performed triple immunostaining for CTCF, STAG1, and STAG2 in human primary skin fibroblasts, chosen for their flat morphology (Fig. 3D–G; Supplemental Movie). We also performed a control using the secondary antibodies only (Supplemental Fig. S6) and a dye-swap as validation (Supplemental Fig. S7A–C). Localization data were analyzed and clustered (Paul et al. 2019), and the resulting binary images were used to infer CTCF, STAG1, and STAG2 coclustering (Fig. 3D–F; Supplemental Fig. S7A,B). We focused on correlations to CTCF clusters, as nearly all CTCF molecules are chromatin-bound (Supplemental Fig. S7F) and the vast majority of cohesin sites are also occupied by CTCF (Fig. 2B).

In our clustered data, we observe CTCF clusters of a mean size of 12,100 nm^2 that are either standalone or overlapped by STAG1- or STAG2-clusters (Fig. 3E,G; Supplemental Fig. S7C). Standalone CTCF clusters consistently showed a size of ~5300 nm^2 (the smallest observed) and represented >50% of all CTCF clusters (Fig. 3F,G). Since CTCF-CTCF loops are typically stabilized by at least one cohesin complex, we postulated that such standalone clusters could represent localization signals from single CTCF molecules. In agreement with this, CTCF dSTORM imaging in RAD21-AID cells showed a reduction in the mean CTCF cluster size from ~11,500 to 6400 nm^2 upon RAD21 degradation (Supplemental Fig. S7D,E), a condition leading to the genome-wide loss of CTCF-CTCF loops (Rao et al. 2017). This reduced cluster size after RAD21 degradation matched that of standalone CTCF clusters in fibroblasts (Fig. 3F).

CTCF clusters overlapping adjacent STAG clusters appear progressively larger, as more STAG1 and/or STAG2 associate with them (ranging from ~8800 for overlap with a single cluster to >50,000 nm^2 for overlap with >5 STAG1/ STAG2 clusters) (Fig. 3F; Supplemental Fig. S7B). This is most likely indicative of higher-order chromatin structures harboring multiple proteins. In agreement with our Re-ChIP data, ~26% CTCF clusters overlap STAG2 and ~10% overlap STAG1, compared to the ~6% overlapping both STAG1 and STAG2 (Fig. 3G). Taken together, these analyses highlight the relative distribution of STAG1- and STAG2-containing cohesin complexes and, to the extent that we record higher-order chromatin interactions, seem to predominantly involve only one of the two STAG proteins.

STAG1 and STAG2 differentially contribute to higher-order chromatin organization

It was previously shown that auxin-induced cohesin degradation alleviates CTCF-CTCF loop formation genome-wide, leading to the profound rearrangement of regulatory chromatin interactions (Rao et al. 2017). Here, we generated highly correlated in situ Hi-C data from two independently obtained STAG1-/ STAG2-AID lines (Supplemental Fig. S8A) that afford higher resolution than previously reported Hi-C from STAG-knockdown cells (Kojic et al. 2018). This allowed us to assess the individual contribution of STAG1 and STAG2 in spatial chromatin organization at different scales.

First, we subtracted Hi-C contact matrices from auxin-treated and untreated cells at a 100-kbp resolution. This revealed changes induced to higher-order chromosomal organization by STAG1 or
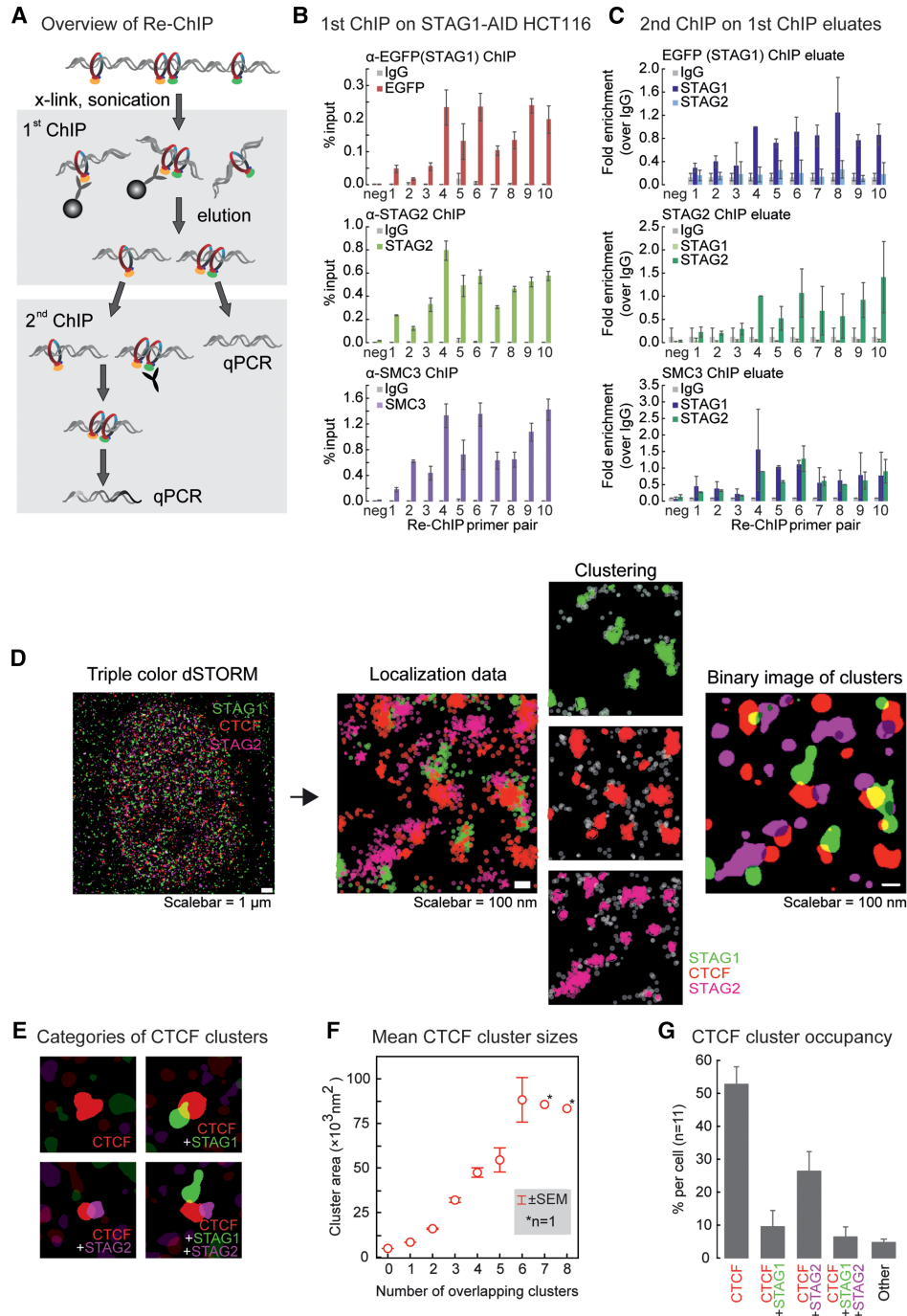
Figure 3. STAG1 and STAG2 do not co-occupy individual binding sites. (*A*) Overview of the Re-ChIP protocol. Please note that in the first ChIP, the antibodies were crosslinked to the beads, allowing for their complete removal from the eluate. (*B*) First ChIP in the Re-ChIP protocol performed from STAG1-AID cells with antibodies against EGFP (to precipitate STAG1), or STAG2 or against SMC3 as a positive control. For the analysis, qPCR primers for the amplification of one negative and 10 positive cohesin binding sites were used (mean and SD from $n = 2$). (*C*) The second ChIP was performed with control IgG, anti-STAG1, and anti-STAG2 antibodies using the eluates from the first ChIP. The same primers as in *B* were used for the analysis. Data are shown as fold enrichment versus IgG; the replicates are further normalized using the positive site #4 (see Methods; mean and SD from $n = 3$ for STAG1 and STAG2, $n = 2$ for SMC3). (*D*) Analysis pipeline of the *d*STORM imaging data. A merged reconstructed triple-color *d*STORM image of a single nucleus stained for STAG1 (green), STAG2 (magenta), and CTCF (red) is shown at the *left* side. For a zoomed region from the same cell, the raw localizations are shown. The result of the kernel density estimation-based clustering algorithm for the individual colors are shown next to it. Not-clustered localizations are depicted in gray. Finally, a binary image of the same region is shown at the *right* with the clusters for all three proteins represented. (*E*) Examples of the four most common groups of CTCF cluster with either: none, one STAG1, one STAG2, or both one STAG1 and one STAG2 cluster adhering. (*F*) The cluster area size (nm²) for CTCF is plotted grouped per number of adherent clusters of STAG1 or STAG2. (*G*) Frequency of CTCF cluster groups per cell measured for 11 cells. All CTCF clusters falling in other groups are depicted as "Others." This group contains 18 subgroups, for example, adhering to more than two clusters or two clusters of the same STAG. All error bars show standard error of the mean (± SEM). Note that in Supplemental Figure S7, the same experiment using different secondary antibodies and different fluorophores is shown.

STAG2 depletion that are not only non-converging but at places display inverse patterns (see examples in Fig. 4A,B and zoom-ins at 25-kb resolution in Fig. 4C, D; Supplemental Fig. S8B). In line with previous observations, we detected no widespread switches between A- and B-compartments upon either depletion (Supplemental Fig. S9A; Seitan et al. 2013; Sofueva et al. 2013; Zuin et al. 2014a; Nora et al. 2017; Rao et al. 2017). Still, a general increase in longer-range interactions (>2 Mb) was seen in STAG1-depleted cells, in contrast to a largely inversed trend in STAG2-depleted ones (Supplemental Fig. S9B).

Looking at the level of individual TADs (up to ~2 Mbp), STAG1 depletion resulted in stronger loss of interactions and general contact reshuffling compared to STAG2 depletion (Fig. 4E; Supplemental Fig. S9C). We identified TAD boundaries with TADtool (Kruse et al. 2016) and found that the majority (~60%) remained unaffected despite STAG1 or STAG2 depletion. Of the ~40% TAD boundaries that did change, in both cases they mostly merge with adjacent TADs (i.e., loss of local insulation in ~20% TADs) or a new boundary develops (in ~15% TADs) (Supplemental Fig. S9D). These effects are consistent with the collapse of loop domains seen upon RAD21 depletion (Rao et al. 2017).

Both TAD number and TAD border strength were more affected by STAG1 depletion (Supplemental Fig. S9E,F), while no significant differences between STAG1 or STAG2 could be observed in TAD border conservation (Supplemental Fig. S9G). Changes in interactions occurring across TAD boundaries strengthened only within the A-compartment upon STAG2 degradation, whereas upon STAG1 depletion, they weakened (and moderately increased in B-compartments) (Supplemental Fig. S9H).

Finally, we plotted average interaction profiles around STAG1/STAG2-shared peaks and STAG1- or STAG2-only peaks (Fig. 4G). In non-auxin-treated cells, STAG1/STAG2-shared peaks and STAG1-only, but not STAG2-only sites, reside at sites of local contact insulation (i.e., at TAD or loop domain boundaries). Upon depletion of either subunit, we again observed shorter-range contact changes around STAG2-only sites and longer-range changes around STAG1-only and STAG1/STAG2-shared sites (Fig. 4G).

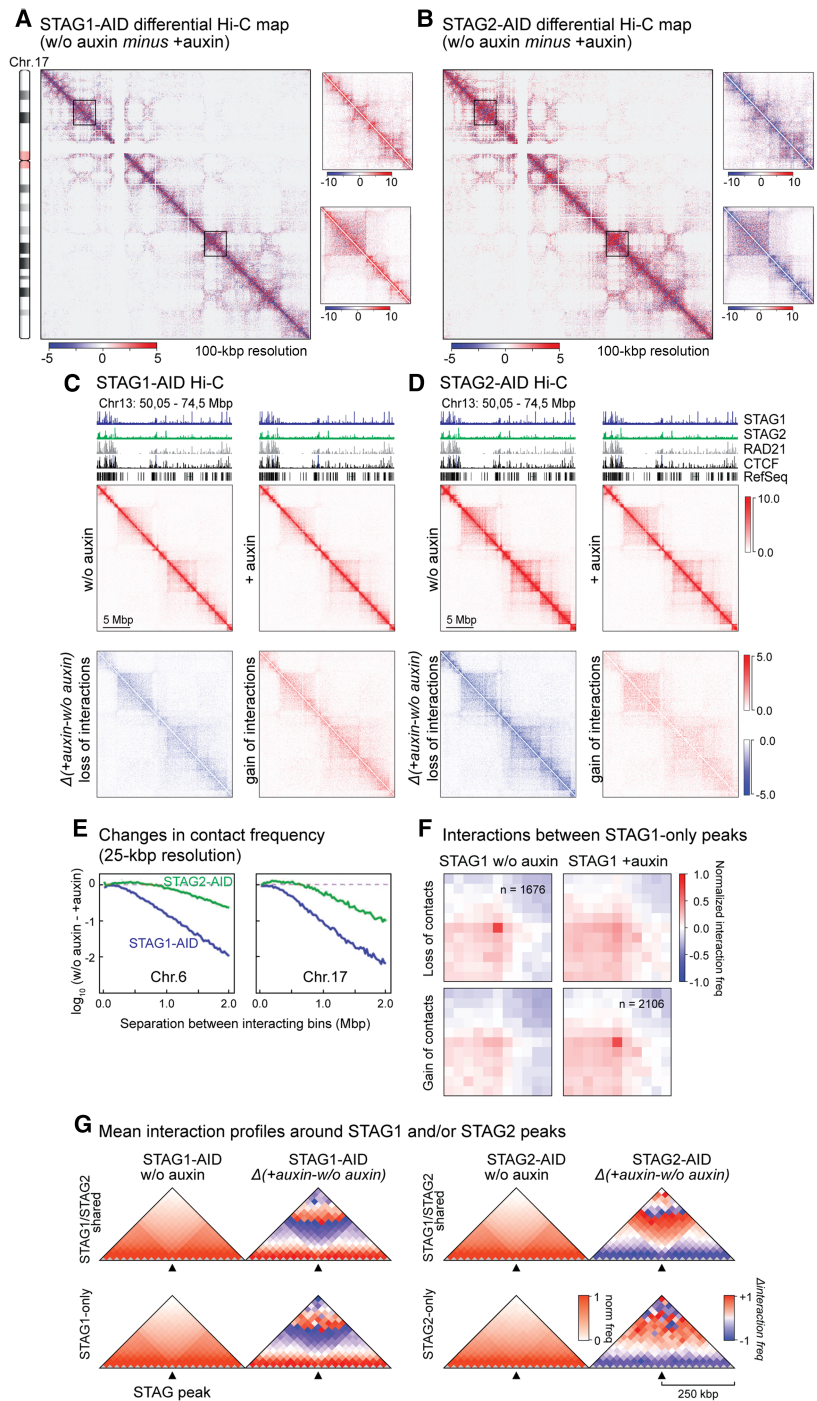We next used the highest (i.e., 10-kbp) resolution our Hi-C data could

Figure 4. Hi-C reveals different contributions of STAG1 and STAG2 to higher-order chromatin structure. (*A,B*) Differential maps of Chromosome 17 illustrating the chromatin contact changes after auxin-mediated degradation of STAG1 (*A*, STAG1-AID) or STAG2 (*B*, STAG2-AID). Examples of changes are encircled. Color key = Balanced (Knight-Ruiz) Hi-C contact frequencies. (*C,D*) Zoom-in for a region of Chromosome 13 into the contact maps for STAG1-AID (*C*) and STAG2-AID (*D*) cells. The maps for untreated cells (w/o auxin), treated cells (+auxin), and the differential interaction maps split in loss of interactions (blue) and gain of interactions (red) are shown. (*E*) Change of chromatin contact frequency relative to the separation of the contacting bins (25 kb) after STAG1 or STAG2 degradation for the examples of Chromosomes 6 and 17. (*F*) Aggregate peak analysis of STAG1-only peaks showing that a lot of the sites lose their respective contacts after STAG1 degradations while alternative contacts are formed. (*G*) Insulation plots showing the averaged Hi-C signals for all STAG1/STAG2 shared peaks as well as all STAG1-only and STAG2-only peaks in the untreated maps (w/o auxin). For the same peaks, the averaged differential Hi-C signals in the different maps are shown. The maps are presented with a bin size of 25 kb and 10 bins to the *left* and *right* of each binding site.

afford to query looping interactions between sites bound by one or the other cohesin-STAG complex. Focusing on STAG1- and STAG2-only peaks, we found STAG2-only peaks did not appear to form loops (with the caveat of their low number of 568 peaks) (Supplemental Fig. S9I). To substantiate this inability, we also asked whether STAG2-only sites might form loops with any other STAG-bound site; we used Fit-Hi-C (Ay et al. 2014) to call all loop-like interactions in our Hi-C matrices and mined those with a STAG2-only peak in at least one of its anchors. This only returned 126 loops of ~0.8 Mbp in size that were also not sensitive to STAG2 auxin-mediated degradation (Supplemental Fig. S9J). In contrast, STAG1-only-bound sites gave rise to >1600 long-range loops in *cis*, which were markedly weakened upon STAG1 degradation (Fig. 4F). Approximately 2000 loops emerge in STAG1-depleted cells connecting previously bound STAG1-only sites (Fig. 4F). These were not seen as strong loops in non-auxin-treated cells, indicating widespread loop rewiring in the absence of STAG1. These two subsets contain 833 loops with STAG1-only shorter-range anchors that persist upon STAG1 degradation (Supplemental Fig. S10A,B). These persistent STAG1-only loops are significantly enriched for convergent CTCF DNA-binding motifs at their anchors, compared to STAG1-only loops detected in the presence or absence of STAG1 (Supplemental Fig. S10C). This is in line with what was shown for strong loops across numerous mammalian cell types (Rao et al. 2014; Guo et al. 2015) cobound by cohesin (Sofueva et al. 2013; Zuin et al. 2014a). Collectively, this analysis highlights reciprocal and subunit-specific contribution of STAG1 and STAG2 to 3D chromatin organization at different scales. At the Mbp-level, STAG1 depletion leads to a stronger contact reshuffling than STAG2, and this remains so at higher resolution, where individual looping events emanating from STAG1-only sites are selectively lost or rewired upon STAG1 depletion. On the other hand, STAG2-only peaks do not contribute significantly to looping and might rather directly affect gene expression, as recently proposed (Kojic et al. 2018).

STAG1 and STAG2 depletion affect distinct gene subsets

Our analyses of genome-wide binding and contribution to chromatin looping indicated that STAG1 and STAG2 might affect gene regulation via distinct paths. This prompted us to identify genes differentially expressed upon depletion of either STAG in HCT116. We performed RNA-seq in two independent STAG1-AID and STAG2-AID clones. After filtering out auxin-responsive loci (Rao et al. 2017), we observed 167 and 169 misregulated genes (FC > 0.6; *P*-value < 0.05) following STAG1 and STAG2 depletion, respectively (Fig. 5A,B; Supplemental Fig. S11A,B). Of these, only 36 were also reported as misregulated by RAD21 degradation in the same cells (Supplemental Fig. S11C; Rao et al. 2017). Most of these gene expression changes were not seen in the reciprocal AID line, as confirmed by RT-qPCR analysis of selected genes (Fig. 5C). This hints at specific roles for STAG1 or STAG2 in gene expression regulation. GO analysis with IPA (Ingenuity Pathway Analysis) (Krämer et al. 2014) revealed that STAG1 and STAG2 control genes belonging to different pathways and networks. For instance, STAG1 depletion affected genes linked to pathways relevant to neuronal development (Supplemental Fig. S11D), as was proposed (Soardi et al. 2017).

To assess the significance of these predictions in a relevant cellular context, we depleted *STAG1*, *STAG2*, or *SMC1A* in human neural stem cells (hNSCs) using siRNAs (Supplemental Fig. S12A–F). We first tested genes misregulated by STAG1 and

STAG2 degradation and confirmed that many genes also depend on STAG1 or STAG2 in this cell type (Fig. 5D), with discrepancies probably due to differential cell type–dependencies. We next tested genes associated with neuronal development and found that their expression depended either on both STAG1 and STAG2 (*CDK6* and *ADAM19*) or only on STAG2 (*AXL*, *IL6ST*, and *GAL*) (Fig. 6). For these genes, an *SMC1A* knockdown was also tested (Supplemental Fig. S12A–C). In summary, many of the gene expression changes documented in our HCT116 model translate into dependencies in a cell type relevant to neural development, with many of the tested genes also implicated in cancer (Mochizuki and Okada 2007; Tigan et al. 2016).

Finally, to understand how STAG1 or STAG2 depletion underpins misregulation of particular gene subsets, we plotted cohesin (RAD21, SMC1A) and CTCF ChIP-seq signals relative to the promoter (transcription start site, TSS) and the 3′ end of STAG1-/STAG2-regulated genes (transcription termination site, TTS) and up to 6 kbp up- and downstream (Supplemental Fig. S13A). For genes down-regulated after STAG1 degradation, we observed enriched cohesin, but not CTCF, signal at the TSS, pointing to a CTCF-independent binding here, as reported for particular promoters before (Schmidt et al. 2010). Genes down-regulated after STAG2 degradation have enriched cohesin and CTCF signal at both the TSS and TTS, suggesting that long-range interactions spanning their gene bodies might be involved in their regulation. Up-regulated genes have cohesin and CTCF signals enriched at their TSS. We speculated that these promoters are now contacting noncognate enhancers due to a reshuffling of promoter-based long-range interactions, in line with the mechanism proposed to follow cohesin degradation (Rao et al. 2017). We plotted average Hi-C profiles around the TSS of these four STAG1-/STAG2-regulated gene subsets (Supplemental Fig. S13B). TSSs of genes up-regulated upon STAG1 or STAG2 depletion do not reside at sites of local insulation (i.e., at a TAD or loop domain boundary), but reshuffling of Hi-C contacts does occur at the longer- and shorter-range, respectively. This effect also holds true for down-regulated genes, but here, there is a stronger indication of them residing at a boundary site remodeled upon STAG1 or STAG2 depletion (Supplemental Fig. S13B). This agrees with the early observation that such boundary sites are often marked by active gene promoters (Dixon et al. 2012), and their down-regulation would then affect boundary strength.

Discussion

While distinct roles for STAG1 and STAG2 have been proposed for their binding at telomeres and centromeres (Canudas and Smith 2009; Bisht et al. 2013), ChIP experiments for these two factors revealed extensive overlap between the two, as well as with CTCF along human chromosomal arms (Fig. 2A; Supplemental Fig. S3; Wendt et al. 2008; Remeseiro et al. 2012). Our ChIP-seq exploited the mClover-tag in the *STAG1* and *STAG2* loci, thereby eliminating antibody bias. We still saw extensive overlap between STAG1 and STAG2 peaks, aligning well to published RAD21 ChIP-seq data from HCT116 (Rao et al. 2017). However, we observed that 26% of all STAG1 and 4% of all STAG2 binding sites did not show binding by the other STAG subunit. These uniquely occupied sites are still co-occupied by CTCF, which contrasts with previous observations of a large number of STAG2-only peaks lacking CTCF (Kojic et al. 2018). This might be attributed to cell type–specific differences, since the relative numbers of STAG1- and STAG2-bound sites differ significantly between cell types (Kojic et al.
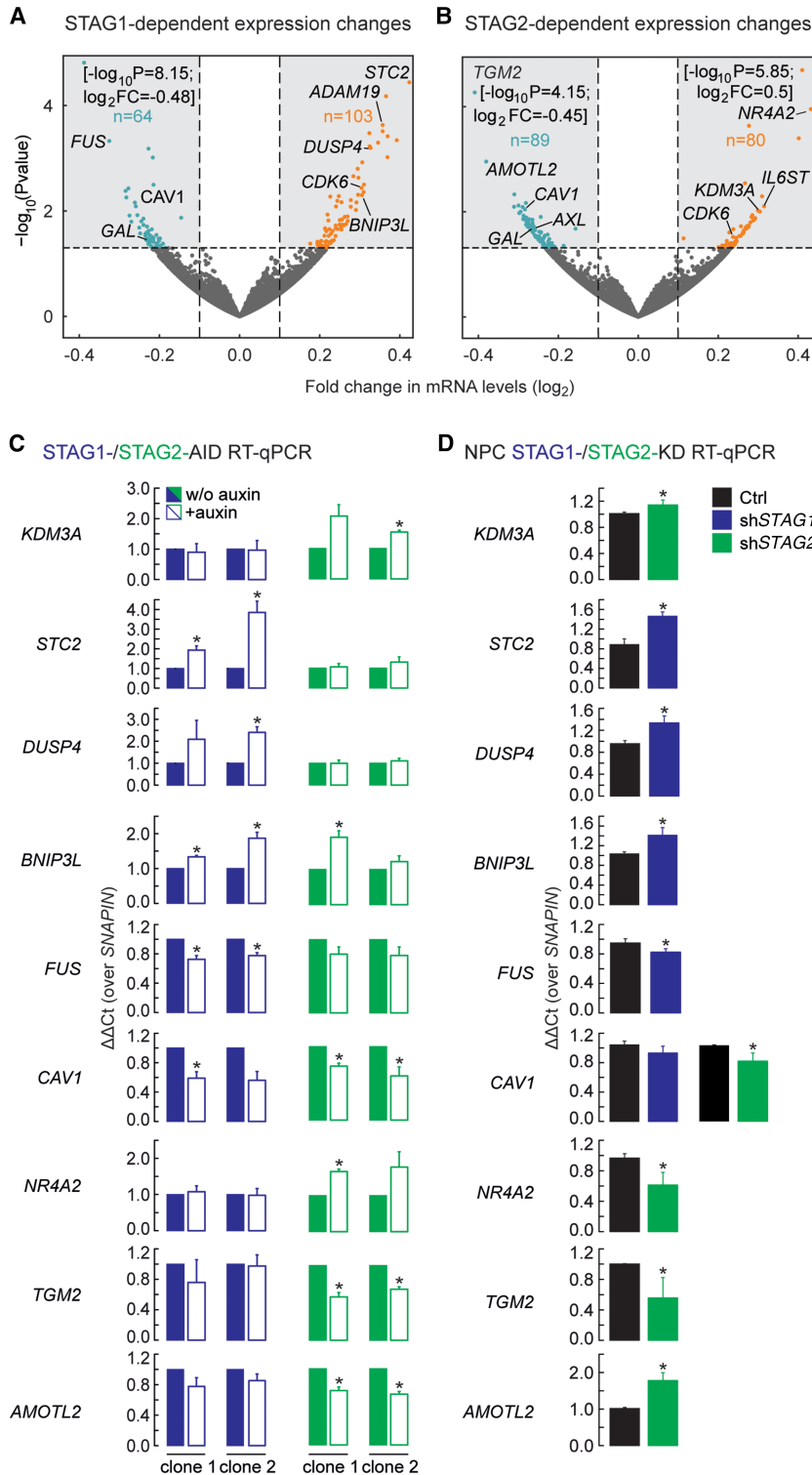
Figure 5. STAG1 or STAG2 regulate different genes. (*A,B*) Volcano plots representing the transcriptional changes after STAG1 degradation (*A*) or STAG2 degradation (*B*). Significantly changing genes are plotted in blue when down-regulated, in orange when up-regulated. Genes that lie outside of the plotted range are indicated with their fold change and *P*-value. (*C*) Validation of genes responding to degradation of STAG1 or STAG2 in two independent clones of the respective AID cells by RT-PCR/qPCR. Genes that respond to STAG1 (*STC2, DUSP4, BNIP3L, FUS*) or STAG2 (*KDM3A, NR4A2, TGM2, AMOTL2*) or both (*CAV1*) were tested. (*D*) Sensitivity of genes to depletion of STAG1 or STAG2 was recapitulated in neural stem cells using siRNA depletion of STAG1 (sh*STAG1*) and STAG2 (sh*STAG2*). Mean of $n = 3$, *t*-test *P*-values are indicated, (*) $P < 0.05$, (**) $P < 0.01$.

2018). However, HeLa cells, which contain substantially more STAG2 than STAG1, show >90% STAG2/CTCF overlap (Hauf et al. 2005; Wendt et al. 2008).

Our Re-ChIP and single-molecule *d*STORM localization experiments revealed that, at the level of single alleles, individual binding sites are actually occupied exclusively by either cohesin-STAG1 or cohesin-STAG2, contradicting recent propositions of cobinding (Kojic et al. 2018). The overlap of STAG1 and STAG2 ChIP-seq peaks then simply reflects the fact that these sites have no preference for STAG1 or STAG2 in the population. STAG1/STAG2-shared sites, as well as STAG1-only but not STAG2-only sites display chromatin insulation properties (Fig. 4G). This agrees with the observation that STAG1/STAG2-shared sites have a similar genomic distribution as STAG1-only sites, in contrast to STAG2-only sites that preferentially localize to gene promoters.

Upon STAG1- or STAG2-degradation, functional differences between STAG1 and STAG2 become apparent also at shared sites. STAG2 depletion leads to a loss of insulation and to a mild, yet notable, increase in shorter-range interactions, visible in both insulation and decay plots (Fig. 4E,G). In contrast, upon STAG1 depletion, we observe reduced interactions at the range of TAD sizes (i.e., up to ~2 Mbp) (Fig. 4E, G). This discrepancy can be interpreted on the basis of (1) the increase in STAG1 occupancy at STAG2-bound sites in the absence of STAG2 that is more pronounced than the converse (Supplemental Fig. S3H–K), and (2) the combination of FRAP studies and loop extrusion modeling that suggest continuous formation and collapse of chromatin loops relying on cohesin and CTCF throughout the cell cycle (Hansen et al. 2017). In other words, introduction of more STAG1 can allow establishment of new loops within Mbp-sized domains. Yet another hint that chromatin interactions change differentially when STAG1 or STAG2 are depleted was provided by Wutz and coworkers in a very recent publication (Wutz et al. 2020). They observed longer chromatin loops after depletion of STAG2 for 48 h, presumably mediated by STAG1. We reanalyzed our Hi-C data accordingly and indeed observed moderately increased loop lengths following STAG2 degradation (Supplemental Fig. S14A–C). We also asked whether the chromatin changes we recorded

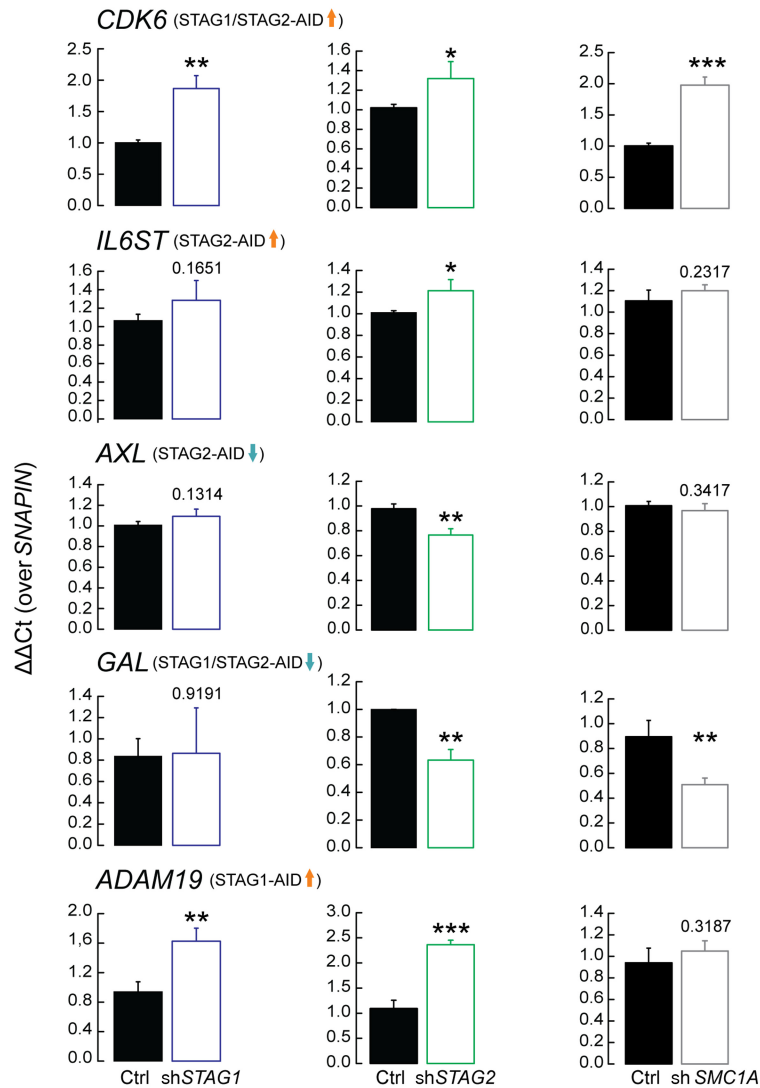## STAG1-/STAG2-relevant gene expression changes in NSCs

Figure 6. STAG1 and STAG2 are important in the regulation of genes involved in neuronal development. Genes found to be involved in neuronal development and misregulated by STAG1 and STAG2 degradation were tested in neural stem cells under control (Ctrl), *STAG1* (sh*STAG1*), *STAG2* (sh*STAG2*), and *SMC1A* (sh*SMC1A*) siRNA knockdown to test whether they depend specifically on STAG1 or STAG2 or on the presence of the cohesin complex in general. The tested genes are: *CDK6*, associated with microcephaly (Faheem et al. 2015); *AXL*, intellectual disability (Burstyn-Cohen 2017); *IL6ST*, neural protection and development (März et al. 1997); *ADAM19*, neurogenesis (Alfandari and Taneyhill 2018); *GAL*, neuro-regulatory peptide-encoding gene (Borroto-Escuela et al. 2017). Mean of $n = 3$; t-test P-values are indicated. (*) $P < 0.05$, (**) $P < 0.01$, (***) $P < 0.001$.

other, >1000 loops form de novo between previously STAG1-only occupied sites. This likely indicates that replacing STAG1 by STAG2 at these sites suffices for loop formation, albeit not without reshuffling loop anchors, since STAG2-only sites form a small number of loops among them or with other STAG1/STAG2 sites (Supplemental Fig. S9I,J). Thus, we suggest that context (i.e., the orientation of the underlying CTCF sites and the repertoire of cobound factors at the anchors of prospective loops) is decisive for chromatin folding via STAG1/2 and determines redundant and unique contributions.

Degradation of STAG1 or STAG2 also led to moderate changes in gene expression (Fig. 5). Most of these genes were specifically affected in response to depletion of one or the other STAG, and not after RAD21 degradation (Rao et al. 2017). This pattern was recapitulated in neural stem cells using siRNA-mediated depletion of either STAG. We suggest that STAG2 has more direct effects on gene transcription due to its higher incidence at gene promoters compared to STAG1 (Fig. 2F), as also proposed by Kojic et al. (2018). On the other hand, the TSS of STAG1-dependent genes generally resided at a position of local insulation, and STAG1 seems to affect formation of longer-range loops (Supplemental Fig. S14). STAG1 depletion might thus cause gene misregulation via redirection of spatial chromatin contacts.

Finally, our *d*STORM imaging revealed—to our knowledge, for the first time—that approximately only half of the observed CTCF clusters are in contact with cohesin in skin fibroblasts. Since, in these cells, the vast majority of CTCFs are chromatin-bound, CTCF clusters not contacting cohesin could represent the nonspecific DNA-binding pool of CTCF observed by FRAP experiments in U2OS cells (Hansen et al. 2017); alternatively, it can be that only a subset of CTCF binding sites in

following STAG1 or STAG2 degradation can also be recapitulated if "wild-type" HCT116 Hi-C is used as a control data set. To this end, we compared our Hi-C data to that from untreated RAD21-AID HCT116 (Rao et al. 2017) and obtained essentially identical changes at all levels of chromatin organization (despite differences in Hi-C preparations and sequencing depth) (Supplemental Fig. S15A–F).

Despite robust and acute degradation of either STAG subunit in our cells, not all loops forming between STAG1-only sites are sensitive to STAG1 degradation. On one hand, there is a subset of ~800 loops that persist despite STAG1 depletion, and on the

a cell are occupied by cohesin at a given time. The size of the CTCF clusters increases as the number of contacting cohesin clusters rises; the CTCF cluster size doubles, for example, when associated with two cohesin clusters. It is thus tempting to speculate that these larger clusters represent CTCF sites engaged in chromatin loops, although we did not directly visualize loops here. This hypothesis is reinforced by our observation that the median CTCF cluster size in RAD21-AID cells (Natsume et al. 2016) decreases upon RAD21 degradation to a size comparable to that of the smallest CTCF clusters in skin fibroblasts. This rules out that larger CTCF clusters are merely neighboring sites

and points to them being triggers that inform 3D chromatin structure.

Taken together, we identified both redundant and nonredundant roles for STAG1 and STAG2 subunits of the cohesin ring complex in looping and ultimately in gene regulation. Of course, much of the current knowledge on how these large protein complexes operate comes from population studies complemented by (but not fully aligned to) single-cell measurements. Thus, in the future, it will be important to bridge this gap and address cell-to-cell variation in cohesin/CTCF function in genome organization.

Methods

Cell lines

STAG1-AID and STAG2-AID cell lines were generated using the HCT116-CMV-OsTIR1 cells obtained from M. Kanemaki using the similar strategy as described (Natsume et al. 2016). Details of the procedure and the sequences of the guide RNAs are in Supplemental Methods.

Cell culture

STAG1-AID and STAG2-AID cells as well as RAD21-AID cells (Natsume et al. 2016) were cultured in McCoy's 5A medium supplemented with 10% charcoal/dextran-treated FBS (HYCLONE, GE Healthcare SH30068.03) and PSG. As was also observed in the RAD21-AID cells, the STAG1-AID and STAG2-AID cells showed reduced protein levels compared to wild type due to leakiness of the degron system. We noticed that it strongly depends on the fetal bovine serum used for culturing the AID-tagged cells (see also Supplemental Fig. S1A,B). Using media supplemented with charcoal/dextran-treated FBS retained AID-tagged proteins best.

To induce protein degradation, 500 µM indole-3-acetic acid (auxin, IAA) dissolved in ethanol or the solvent ethanol as a control were added for 12 h.

Human primary skin fibroblasts (Dept. of Clinical Genetics, Erasmus MC) were cultured in DMEM medium with 10% FBS and PSG.

Antibodies

Rabbit polyclonal antibodies directed against EGFP, STAG1, and STAG2 were custom-made. Details for antibody generation are in Supplemental Methods. The anti-SMC3 antibody has been described before (Zuin et al. 2014b). Additional antibodies are listed in Supplemental Table S1.

Immunoprecipitation

Immunoprecipitation experiments were performed as described (Watrin et al. 2006).

Cell fractionation

Whole-cell extracts of human primary skin fibroblasts were separated into soluble supernatant and chromatin-containing pellet fractions as described (Watrin et al. 2006).

ChIP sample preparation

ChIP was performed as described (Cabianca et al. 2012) with some adaptations. Details are in Supplemental Methods. For indicated experiments, the OneDay ChIP kit (Diagenode) was used according to the protocol of the manufacturer. The samples were either analyzed by qPCR (the respective primers are listed in Supplemental Table S2) or processed for sequencing.

ChIP-seq sample preparation and sequencing

Details about ChIP-seq sample preparation and sequencing are in Supplemental Methods.

ChIP-seq analysis

Details for initial ChIP-seq analysis are in Supplemental Methods. Sequencing data information and statistics are shown in Supplemental Table S6. All software used for the analysis is listed in Supplemental Table S9.

Cohesin positions (common, STAG1-only, and STAG2-only sites) were defined by calculating the overlap between STAG1 and STAG2 peaks using the "intersect" option of BEDTools v2.27 (Quinlan and Hall 2010) with a minimum of 1-nt overlap. STAG1 peaks called using a q-value of 0.005 were intersected with STAG2 peaks called using a q-value of 0.06 to define STAG1-only sites. For STAG2-only sites, a list of STAG2 peaks (q-value = 0.05) was intersected with a list of STAG1 sites (q-value = 0.06).

Mean read density profiles and read density heat maps were obtained with deepTools (Ramírez et al. 2016) using normalized bigWig files and plotting them around peak summits of STAG1- or STAG2-only or common peaks. For the SMC3 heat maps, input-normalized bigWig files were used.

Details about the analysis of the enrichment of common and -only sites at enhancer and promoters are in Supplemental Methods.

Transcription factor mapping

The analysis of transcription factor motifs at STAG1 and STAG2 binding sites in context with DNase hypersensitivity as a marker for the accessibility of these predicted TF sites was performed as described previously (Lin et al. 2015).

Culturing of neural stem cells and siRNA knockdown

Culturing of human neural stem cells and siRNA knockdown preparation were performed as described in Kruszka et al. (2019). Details and siRNA sequences are in Supplemental Methods.

Transcription analysis by reverse transcription (RT) and qPCR

Details about RNA and cDNA preparation and transcription analysis are in Supplemental Methods. The sequences of the primers used for the RT-qPCR are listed in Supplemental Table S3.

Re-ChIP or sequential ChIP

The original protocol from Völkel et al. (2015) was modified to perform the first ChIP step with antibodies crosslinked to beads. To prepare the beads, 20 mg of the different antibodies were loaded on 50 µL Affi-Prep Protein A Resin (Bio-Rad) (multiply this with the number of second ChIP's planned and plan one extra sample to check the ChIP efficiency of the first ChIP step). After three washes with TBS/T (0.01% Triton X-100), the beads were washed three times with 0.2 M sodium borate pH 9.0 and then incubated for 20 min with a 20 mM solution of dimethyl pimelimidate dihydrochloride (Sigma-Aldrich) at room temperature under rotation. The crosslinking reaction was quenched by washing the beads three times with 250 mM Tris pH 8.0. Not-crosslinked antibodies were removed by a short treatment with 50 µL 100 mM glycine pH 2.0 per 50 µL beads, and then the beads were neutralized again by washing with TBS/T.

Sample preparation for the chromatin immunoprecipitation was performed as described before (Wendt et al. 2008; Zuin et al. 2014b). Refer to Supplemental Methods for details.

The samples for the second ChIP were eluted with Re-ChIP elution buffer (100 mM NaHCO₃, 1% SDS, 10 mM DTT) twice for 30 min at 37°C with 25 μL per 50 μL beads. The eluates were diluted 1:50 with ChIP buffer from the OneDay ChIP kit (Diagenode) and subsequently subjected to a second ChIP in accordance with the OneDay ChIP kit manual but performing an overnight antibody incubation under rotation at 4°C. Bead washes and cleanup were performed as described in the OneDay ChIP kit protocol. Primer sequences for ChIP-qPCR primers are listed in Supplemental Table S2. The fold enrichment values of the second ChIP depend on the efficiency of the first ChIP. To normalize for these variations and efficiently compare the three experiments, we used the qPCR primer pair #4 to normalize the experiments similarly to what has been previously described (Jermann et al. 2014). Therefore, for this primer pair, no standard deviation is shown.

RNA sample preparation and sequencing

Details about RNA sample preparation and sequencing are in Supplemental Methods.

RNA-seq analysis

Details about RNA-seq analysis are in Supplemental Methods. Sequencing data information and statistics are shown in Supplemental Table S6. All software used for the analysis is listed in Supplemental Table S9.

Genes with an FDR < 0.05 and an absolute ($\log_2$) fold-change of >0.6 were deemed as differentially expressed and listed in Supplemental Tables S4 and S5. Volcano plots were generated using R (https://www.R-project.org/) (R Core Team 2018). Significant deregulated genes (P-value > 0.05) were labeled in green. Genes found to be deregulated in both cases, after depletion of STAG1 and STAG2, where labeled in blue. Gene Ontology and networks were generated through Metascape (Zhou et al. 2019).

Hi-C sample preparation, sequencing, and data analysis

In situ Hi-C data from STAG1-/STAG2-AID HTC116 cells were generated as described previously (Zirkel et al. 2018) in two biological replicates each. For Hi-C sample sequencing and data analysis, details are in Supplemental Methods. Sequencing data information and statistics are shown in Supplemental Table S6. All software used for this analysis is listed in Supplemental Table S9. All in-house programming scripts used for the analysis were written in Python v2.7.15rc1 (https://www.python.org/) and R v.3.3.4 (https://www.R-project.org/) (R Core Team 2018) and are available at GitHub (https://github.com) in the repository https://github.com/eggduzao/Casa_et_al (under GNU General Public License v3.0).

Immunostaining (including dSTORM preparation)

A detailed description of the immunostaining procedure is present at Supplemental Methods. A list of all antibodies used is shown at Supplemental Table S1.

dSTORM imaging

Cells were seeded to 70% density on cover slips; fixed and stained cells were mounted in an Attofluor cell chamber (Thermo Fisher Scientific) and in 1 mL of dSTORM buffer (25 mM MEA, glucose oxidase, catalase [all from Sigma-Aldrich], 50 mM NaCl, and 10% glucose [Sigma-Aldrich] in 10 mM Tris-HCl pH 8.0). The cell chamber was sealed with a cover slip and incubated on the microscope at room temperature for 30 min prior to imaging, to minimize drift. Imaging was performed using a Zeiss Elyra PS1 system fitted with an Andor iXon DU 897, 512 × 512 EMCCD camera. Images were made using a 100× 1.49NA TIRF objective and were imaged in HiLo mode. High Power 100 mW diode lasers with wavelengths of 488, 561, and 642 nm were used to excite the fluorophores and, respectively, BP495-575 + LP750, BP 570-650 + LP750, or LP655 filters were used. Movies of 12,000 frames were recorded with an exposure time of 33 msec. Multichannel images were acquired sequentially from high wavelength to lower wavelengths. In the Supplemental Movie, 1000 frames from one of the experiments are shown.

dSTORM analysis

Three dSTORM movies were made, one for each protein, and analyzed using Zeiss ZEN 2012 software. Localizations with a precision larger than 50 nm were discarded; remaining localizations were drift-corrected using a model-based approach. All additional analysis was done in R (https://www.R-project.org/) (R Core Team 2018) using the SMoLR package v.1.0.3 (Paul et al. 2019) and Fiji (Schindelin et al. 2012). Localizations from a single nucleus were selected manually by selecting a region of interest (ROI) in Fiji and the IJROI_subset function in SMoLR. Localizations were clustered based on their density using a kernel density estimation (KDE)-based clustering algorithm with the threshold set to 0.05 for all three channels. All clusters for CTCF were selected, and their area was measured using the thresholded KDE binary image. In the triple channel dSTORM experiments, CTCF was grouped based on the number of overlapping binary clusters from the STAG1 and STAG2 channels; clusters were considered overlapping if pixels containing both colors were present in the structure.

Data access

All raw and processed sequencing data generated in this study have been submitted to the NCBI Gene Expression Omnibus (GEO; https://www.ncbi.nlm.nih.gov/geo/) under accession number GSE132014. All in-house code/scripts used to perform the analyses are available at GitHub (https://github.com/eggduzao/Casa_et_al) (under GNU General Public License v3.0) and as Supplemental Code.

Competing interest statement

The authors declare no competing interests.

Acknowledgments

References

Alfandari D, Taneyhill LA. 2018. Cut loose and run: the complex role of ADAM proteases during neural crest cell development. *Genesis* **56**: e23095. doi:10.1002/dvg.23095

Ay F, Bailey TL, Noble WS. 2014. Statistical confidence estimation for Hi-C data reveals regulatory chromatin contacts. *Genome Res* **24**: 999–1011. doi:10.1101/gr.160374.113

Balbás-Martínez C, Sagrera A, Carrillo-de-Santa-Pau E, Earl J, Márquez M, Vazquez M, Lapi E, Castro-Giner F, Beltran S, Bayés A, et al. 2013. Recurrent inactivation of *STAG2* in bladder cancer is not associated with aneuploidy. *Nat Genet* **45**: 1464–1469. doi:10.1038/ng.2799

Benedetti L, Cereda M, Monteverde L, Desai N, Ciccarelli FD. 2017. Synthetic lethal interaction between the tumour suppressor *STAG2* and its paralog *STAG1*. *Oncotarget* **8**: 37619–37632. doi:10.18632/oncotarget.16838

Bisht KK, Daniloski Z, Smith S. 2013. SA1 binds directly to DNA through its unique AT-hook to promote sister chromatid cohesion at telomeres. *J Cell Sci* **126**: 3493–3503. doi:10.1242/jcs.130872

Borroto-Escuela DO, Carlsson J, Ambrogini P, Narváez M, Wydra K, Tarakanov AO, Li X, Millón C, Ferraro L, Cuppini R, et al. 2017. Understanding the role of GPCR heteroreceptor complexes in modulating the brain networks in health and disease. *Front Cell Neurosci* **11**: 37. doi:10.3389/fncel.2017.00037

Brohl AS, Solomon DA, Chang W, Wang J, Song Y, Sindiri S, Patidar R, Hurd L, Chen L, Shern JF, et al. 2014. The genomic landscape of the Ewing sarcoma family of tumors reveals recurrent *STAG2* mutation. *PLoS Genet* **10**: e1004475. doi:10.1371/journal.pgen.1004475

Burstyn-Cohen T. 2017. TAM receptor signaling in development. *Int J Dev Biol* **61**: 215–224. doi:10.1387/ijdb.160285tb

Busslinger GA, Stocsits RR, van der Lelij P, Axelsson E, Tedeschi A, Galjart N, Peters JM. 2017. Cohesin is positioned in mammalian genomes by transcription, CTCF and Wapl. *Nature* **544**: 503–507. doi:10.1038/nature22063

Cabianca DS, Casa V, Bodega B, Xynos A, Ginelli E, Tanaka Y, Gabellini D. 2012. A long ncRNA links copy number variation to a polycomb/trithorax epigenetic switch in FSHD muscular dystrophy. *Cell* **149**: 819–831. doi:10.1016/j.cell.2012.03.035

Canudas S, Smith S. 2009. Differential regulation of telomere and centromere cohesion by the Scc3 homologues SA1 and SA2, respectively, in human cells. *J Cell Biol* **187**: 165–173. doi:10.1083/jcb.200903096

Deng Z, Wang Z, Stong N, Plasschaert R, Moczan A, Chen HS, Hu S, Wikramasinghe P, Davuluri RV, Bartolomei MS, et al. 2012. A role for CTCF and cohesin in subtelomere chromatin organization, TERRA transcription, and telomere end protection. *EMBO J* **31**: 4165–4178. doi:10.1038/emboj.2012.266

Dixon JR, Selvaraj S, Yue F, Kim A, Li Y, Shen Y, Hu M, Liu JS, Ren B. 2012. Topological domains in mammalian genomes identified by analysis of chromatin interactions. *Nature* **485**: 376–380. doi:10.1038/nature11082

Faheem M, Naseer MI, Rasool M, Chaudhary AG, Kumosani TA, Ilyas AM, Pushparaj P, Ahmed F, Algahtani HA, Al-Qahtani MH, et al. 2015. Molecular genetics of human primary microcephaly: an overview. *BMC Med Genomics* **8**: S4. doi:10.1186/1755-8794-8-S1-S4

Guo Y, Xu Q, Canzio D, Shou J, Li J, Gorkin DU, Jung I, Wu H, Zhai Y, Tang Y, et al. 2015. CRISPR inversion of CTCF sites alters genome topology and enhancer/promoter function. *Cell* **162**: 900–910. doi:10.1016/j.cell.2015.07.038

Hadjur S, Williams LM, Ryan NK, Cobb BS, Sexton T, Fraser P, Fisher AG, Merkenschlager M. 2009. Cohesins form chromosomal *cis*-interactions at the developmentally regulated *IFNG* locus. *Nature* **460**: 410–413. doi:10.1038/nature08079

Hansen AS, Pustova I, Cattoglio C, Tjian R, Darzacq X. 2017. CTCF and cohesin regulate chromatin loop stability with distinct dynamics. *eLife* **6**: e25776. doi:10.7554/eLife.25776

Hauf S, Roitinger E, Koch B, Dittrich CM, Mechtler K, Peters JM. 2005. Dissociation of cohesin from chromosome arms and loss of arm cohesion during early mitosis depends on phosphorylation of SA2. *PLoS Biol* **3**: e69. doi:10.1371/journal.pbio.0030069

Hill VK, Kim JS, Waldman T. 2016. Cohesin mutations in human cancer. *Biochim Biophys Acta* **1866**: 1–11. doi:10.1016/j.bbcan.2016.05.002

Jermann P, Hoerner L, Burger L, Schubeler D. 2014. Short sequences can efficiently recruit histone H3 lysine 27 trimethylation in the absence of enhancer activity and DNA methylation. *Proc Natl Acad Sci* **111**: E3415–E3421. doi:10.1073/pnas.1400672111

Kojic A, Cuadrado A, De Koninck M, Giménez-Llorente D, Rodríguez-Corsino M, Gómez-López G, Le Dily F, Marti-Renom MA, Losada A. 2018. Distinct roles of cohesin-SA1 and cohesin-SA2 in 3D chromosome organization. *Nat Struct Mol Biol* **25**: 496–504. doi:10.1038/s41594-018-0070-4

Kong X, Ball AR Jr, Pham HX, Zeng W, Chen HY, Schmiesing JA, Kim JS, Berns M, Yokomori K. 2014. Distinct functions of human cohesin-SA1 and cohesin-SA2 in double-strand break repair. *Mol Cell Biol* **34**: 685–698. doi:10.1128/MCB.01503-13

Krämer A, Green J, Pollard J Jr, Tugendreich S. 2014. Causal analysis approaches in Ingenuity Pathway Analysis. *Bioinformatics* **30**: 523–530. doi:10.1093/bioinformatics/btt703

Kruse K, Hug CB, Hernández-Rodríguez B, Vaquerizas JM. 2016. TADtool: visual parameter identification for TAD-calling algorithms. *Bioinformatics* **32**: 3190–3192. doi:10.1093/bioinformatics/btw368

Kruszka P, Berger SI, Casa V, Dekker MR, Gaesser J, Weiss K, Martinez AF, Murdock DR, Louie RJ, Prijoles EJ, et al. 2019. Cohesin complex-associated holoprosencephaly. *Brain* **142**: 2631–2643. doi:10.1093/brain/awz210

Lehalle D, Mosca-Boidron AL, Begtrup A, Boute-Benejean O, Charles P, Cho MT, Clarkson A, Devinsky O, Duffourd Y, Duplomb-Jego L, et al. 2017. *STAG1* mutations cause a novel cohesinopathy characterised by unspecific syndromic intellectual disability. *J Med Genet* **54**: 479–488. doi:10.1136/jmedgenet-2016-104468

Lennox KA, Behlke MA. 2016. Cellular localization of long non-coding RNAs affects silencing by RNAi more than by antisense oligonucleotides. *Nucleic Acids Res* **44**: 863–877. doi:10.1093/nar/gkv1206

Lin Q, Chauvistré H, Costa IG, Gusmao EG, Mitzka S, Hänzelmann S, Baying B, Klisch T, Moriggl R, Hennuy B, et al. 2015. Epigenetic program and transcription factor circuitry of dendritic cell development. *Nucleic Acids Res* **43**: 9680–9693. doi:10.1093/nar/gkv1056

Losada A, Yokochi T, Kobayashi R, Hirano T. 2000. Identification and characterization of SA/Scc3p subunits in the *Xenopus* and human cohesin complexes. *J Cell Biol* **150**: 405–416. doi:10.1083/jcb.150.3.405

März P, Herget T, Lang E, Otten U, Rose-John S. 1997. Activation of gp 130 by IL-6/soluble IL-6 receptor induces neuronal differentiation. *Eur J Neurosci* **9**: 2765–2773. doi:10.1111/j.1460-9568.1997.tb01705.x

Mochizuki S, Okada Y. 2007. ADAMs in cancer cell proliferation and progression. *Cancer Sci* **98**: 621–628. doi:10.1111/j.1349-7006.2007.00434.x

Mullegama SV, Klein SD, Mulatinho MV, Senaratne TN, Singh K, UCLA Clinical Genomics Center, Nguyen DC, Gallant NM, Strom SP, Ghahremani S, et al. 2017. De novo loss-of-function variants in *STAG2* are associated with developmental delay, microcephaly, and congenital anomalies. *Am J Med Genet A* **173**: 1319–1327. doi:10.1002/ajmg.a.38207

Nativio R, Wendt KS, Ito Y, Huddleston JE, Uribe-Lewis S, Woodfine K, Krueger C, Reik W, Peters JM, Murrell A. 2009. Cohesin is required for higher-order chromatin conformation at the imprinted *IGF2-H19* locus. *PLoS Genet* **5**: e1000739. doi:10.1371/journal.pgen.1000739

Natsume T, Kiyomitsu T, Saga Y, Kanemaki MT. 2016. Rapid protein depletion in human cells by auxin-inducible degron tagging with short homology donors. *Cell Rep* **15**: 210–218. doi:10.1016/j.celrep.2016.03.001

Nishiyama T. 2019. Cohesion and cohesin-dependent chromatin organization. *Curr Opin Cell Biol* **58**: 8–14. doi:10.1016/j.ceb.2018.11.006

Nora EP, Lajoie BR, Schulz EG, Giorgetti L, Okamoto I, Servant N, Piolot T, van Berkum NL, Meisig J, Sedat J, et al. 2012. Spatial partitioning of the regulatory landscape of the X-inactivation centre. *Nature* **485**: 381–385. doi:10.1038/nature11049

Nora EP, Goloborodko A, Valton AL, Gibcus JH, Uebersohn A, Abdennur N, Dekker J, Mirny LA, Bruneau BG. 2017. Targeted degradation of CTCF decouples local insulation of chromosome domains from genomic compartmentalization. *Cell* **169**: 930–944.e22. doi:10.1016/j.cell.2017.05.004

Paul MW, de Gruiter HM, Lin Z, Baarends WM, van Cappellen WA, Houtsmuller AB, Slotman JA. 2019. SMoLR: visualization and analysis of single-molecule localization microscopy data in R. *BMC Bioinformatics* **20**: 30. doi:10.1186/s12859-018-2578-3

Prieto I, Suja JA, Pezzi N, Kremer L, Martínez AC, Rufas JS, Barbero JL. 2001. Mammalian STAG3 is a cohesin specific to sister chromatid arms in meiosis I. *Nat Cell Biol* **3**: 761–766. doi:10.1038/35087082

Quinlan AR, Hall IM. 2010. BEDTools: a flexible suite of utilities for comparing genomic features. *Bioinformatics* **26:** 841–842. doi:10.1093/bioinformatics/btq033

Ramírez F, Ryan DP, Grüning B, Bhardwaj V, Kilpert F, Richter AS, Heyne S, Dündar F, Manke T. 2016. deepTools2: a next generation web server for deep-sequencing data analysis. *Nucleic Acids Res* **44:** W160–W165. doi:10.1093/nar/gkw257

Rao SS, Huntley MH, Durand NC, Stamenova EK, Bochkov ID, Robinson JT, Sanborn AL, Machol I, Omer AD, Lander ES, et al. 2014. A 3D map of the human genome at kilobase resolution reveals principles of chromatin looping. *Cell* **159:** 1665–1680. doi:10.1016/j.cell.2014.11.021

Rao SSP, Huang SC, Glenn St Hilaire B, Engreitz JM, Perez EM, Kieffer-Kwon KR, Sanborn AL, Johnstone SE, Bascom GD, Bochkov ID, et al. 2017. Cohesin loss eliminates all loop domains. *Cell* **171:** 305–320.e24. doi:10.1016/j.cell.2017.09.026

R Core Team. 2018. *R: a language and environment for statistical computing*. R Foundation for Statistical Computing, Vienna. https://www.R-project.org/.

Remeseiro S, Cuadrado A, Gómez-López G, Pisano DG, Losada A. 2012. A unique role of cohesin-SA1 in gene regulation and development. *EMBO J* **31:** 2090–2102. doi:10.1038/emboj.2012.60

Rocquain J, Gelsi-Boyer V, Adélaïde J, Murati A, Carbuccia N, Vey N, Birnbaum D, Mozziconacci MJ, Chaffanet M. 2010. Alteration of cohesin genes in myeloid diseases. *Am J Hematol* **85:** 717–719. doi:10.1002/ajh.21798

Rubio ED, Reiss DJ, Welcsh PL, Disteche CM, Filippova GN, Baliga NS, Aebersold R, Ranish JA, Krumm A. 2008. CTCF physically links cohesin to chromatin. *Proc Natl Acad Sci* **105:** 8309–8314. doi:10.1073/pnas.0801273105

Schindelin J, Arganda-Carreras I, Frise E, Kaynig V, Longair M, Pietzsch T, Preibisch S, Rueden C, Saalfeld S, Schmid B, et al. 2012. Fiji: an open-source platform for biological-image analysis. *Nat Methods* **9:** 676–682. doi:10.1038/nmeth.2019

Schmidt D, Schwalie PC, Ross-Innes CS, Hurtado A, Brown GD, Carroll JS, Flicek P, Odom DT. 2010. A CTCF-independent role for cohesin in tissue-specific transcription. *Genome Res* **20:** 578–588. doi:10.1101/gr.100479.109

Seitan V, Faure A, Zhan Y, McCord R, Lajoie B, Ing-Simmons E, Lenhard B, Giorgetti L, Heard E, Fisher A, et al. 2013. Cohesin-based chromatin interactions enable regulated gene expression within pre-existing architectural compartments. *Genome Res* **23:** 2066–2077. doi:10.1101/gr.161620.113

Soardi FC, Machado-Silva A, Linhares ND, Zheng G, Qu Q, Pena HB, Martins TMM, Vieira HGS, Pereira NB, Melo-Minardi RC, et al. 2017. Familial *STAG2* germline mutation defines a new human cohesinopathy. *NPJ Genom Med* **2:** 7. doi:10.1038/s41525-017-0009-4

Sofueva S, Yaffe E, Chan WC, Georgopoulou D, Rudan MV, Mira-Bontenbal H, Pollard SM, Schroth GP, Tanay A, Hadjur S. 2013. Cohesin-mediated interactions organize chromosomal domain architecture. *EMBO J* **32:** 3119–3129. doi:10.1038/emboj.2013.237

Solomon DA, Kim JS, Bondaruk J, Shariat SF, Wang ZF, Elkahloun AG, Ozawa T, Gerard J, Zhuang D, Zhang S, et al. 2013. Frequent truncating mutations of *STAG2* in bladder cancer. *Nat Genet* **45:** 1428–1430. doi:10.1038/ng.2800

Tigan AS, Bellutti F, Kollmann K, Tebb G, Sexl V. 2016. CDK6—a review of the past and a glimpse into the future: from cell-cycle control to transcriptional regulation. *Oncogene* **35:** 3083–3091. doi:10.1038/onc.2015.407

Tirode F, Surdez D, Ma X, Parker M, Le Deley MC, Bahrami A, Zhang Z, Lapouble E, Grossetete-Lalami S, Rusch M, et al. 2014. Genomic landscape of Ewing sarcoma defines an aggressive subtype with co-association of *STAG2* and *TP53* mutations. *Cancer Discov* **4:** 1342–1353. doi:10.1158/2159-8290.CD-14-0622

van de Linde S, Löschberger A, Klein T, Heidbreder M, Wolter S, Heilemann M, Sauer M. 2011. Direct stochastic optical reconstruction microscopy with standard fluorescent probes. *Nat Protoc* **6:** 991–1009. doi:10.1038/nprot.2011.336

van der Lelij P, Lieb S, Jude J, Wutz G, Santos CP, Falkenberg K, Schlattl A, Ban J, Schwentner R, Hoffmann T, et al. 2017. Synthetic lethality between the cohesin subunits *STAG1* and *STAG2* in diverse cancer contexts. *eLife* **6:** e26980. doi:10.7554/eLife.26980

Völkel S, Stielow B, Finkernagel F, Stiewe T, Nist A, Suske G. 2015. Zinc finger independent genome-wide binding of Sp2 potentiates recruitment of histone-fold protein Nf-y distinguishing it from Sp1 and Sp3. *PLoS Genet* **11:** e1005102. doi:10.1371/journal.pgen.1005102

Watrin E, Schleiffer A, Tanaka K, Eisenhaber F, Nasmyth K, Peters JM. 2006. Human Scc4 is required for cohesin binding to chromatin, sister-chromatid cohesion, and mitotic progression. *Curr Biol* **16:** 863–874. doi:10.1016/j.cub.2006.03.049

Wendt KS, Yoshida K, Itoh T, Bando M, Koch B, Schirghuber E, Tsutsumi S, Nagae G, Ishihara K, Mishiro T, et al. 2008. Cohesin mediates transcriptional insulation by CCCTC-binding factor. *Nature* **451:** 796–801. doi:10.1038/nature06634

Winters T, McNicoll F, Jessberger R. 2014. Meiotic cohesin STAG3 is required for chromosome axis formation and sister chromatid cohesion. *EMBO J* **33:** 1256–1270. doi:10.1002/embj.201387330

Wutz G, Ladurner R, St Hilaire BG, Stocsits RR, Nagasaka K, Pignard B, Sanborn A, Tang W, Várnai C, Ivanov MP, et al. 2020. ESCO1 and CTCF enable formation of long chromatin loops by protecting cohesin^{STAG1} from WAPL. *eLife* **9:** e52091. doi:10.7554/eLife.52091

Yesbolatova A, Natsume T, Hayashi KI, Kanemaki MT. 2019. Generation of conditional auxin-inducible degron (AID) cells and tight control of degron-fused proteins using the degradation inhibitor auxinole. *Methods* **164-165:** 73–80. doi:10.1016/j.ymeth.2019.04.010

Zhou Y, Zhou B, Pache L, Chang M, Khodabakhshi AH, Tanaseichuk O, Benner C, Chanda SK. 2019. Metascape provides a biologist-oriented resource for the analysis of systems-level datasets. *Nat Commun* **10:** 1523. doi:10.1038/s41467-019-09234-6

Zirkel A, Nikolic M, Sofiadis K, Mallm JP, Brackley CA, Gothe H, Drechsel O, Becker C, Altmüller J, Josipovic N, et al. 2018. HMGB2 loss upon senescence entry disrupts genomic organization and induces CTCF clustering across cell types. *Mol Cell* **70:** 730–744.e6. doi:10.1016/j.molcel.2018.03.030

Zuin J, Dixon JR, van der Reijden MIJA, Ye Z, Kolovos P, Brouwer RWW, van de Corput HJG, van de Werken HJG, Knoch TA, van IJcken WFJ, et al. 2014a. Cohesin and CTCF differentially affect chromatin architecture and gene expression in human cells. *Proc Natl Acad Sci* **111:** 996–1001. doi:10.1073/pnas.1317788111

Zuin J, Franke V, van Ijcken WF, van der Sloot A, Krantz ID, van der Reijden MI, Nakato R, Lenhard B, Wendt KS. 2014b. A cohesin-independent role for NIPBL at promoters provides insights in CdLS. *PLoS Genet* **10:** e1004153. doi:10.1371/journal.pgen.1004153